ISSN 0036-0236, Russian Journal of Inorganic Chemistry, 2024. © Pleiades Publishing, Ltd., 2024.

THEORETICAL
INORGANIC CHEMISTRY

Derivation of a Force Field for Computer Simulations of Multi-Walled Nanotubes. II. Tungsten Diselenide

A. V. Bandura[a], *, S. I. Lukyanov[a], A. V. Domnin[a], D. D. Kuruch[a], and R. A. Evarestov[a]

[a] *Quantum Chemistry Department, Saint-Petersburg State University, St. Petersburg, 199034 Russia*

**e-mail: a.bandura@spbu.ru*

Received June 14, 2024; revised July 14, 2024; accepted July 22, 2024

Abstract—We propose a force field designed to model multi-walled WSe_2 nanotubes whose size is beyond the capabilities of ab initio methods. The parameterization of interatomic potentials is successfully tested on single-walled and double-walled nanotubes, the structure of which is determined using non-empirical calculations. This force field has been used to model the structure and stability of chiral and achiral multi-walled WSe_2 nanotubes with diameters approaching experimental values. The properties of WSe_2-based nanotubes are compared with the properties of analogous WS_2-based nanotubes calculated using the force field, which was published in the previous paper I of this series. The interwall distances obtained from the simulations are in good agreement with recent measurements of these parameters for existing WS_2 and WSe_2 nanotubes. It is found that the interwall interaction contributes to the stabilization of multi-walled nanotubes slightly more in the case of WSe_2 than in the case of WS_2. Analysis of the deviation of the nanotube shape from the cylindrical one showed a close similarity of the structure of the tubes of both compositions.

Keywords: interatomic potentials, multiobjective optimization, genetic algorithms, multi-walled nanotubes, binding energy, strain energy, DFT calculations

DOI: 10.1134/S003602362460268X

INTRODUCTION

Currently, the study of transition metal dichalcogenide structures with reduced periodicity, mainly nanolayers and nanotubes, is carried out with high intensity [1, 2] because of the scientific interest in fundamental knowledge, since the reduction of the periodicity of crystalline systems leads to the emergence of new physical phenomena [3, 4]. New phenomena, in turn, give rise to new advances in the applied fields of nano- and optoelectronics [5–7].

Most studies of nanotubes based on transition metal dichalcogenides have focused on the structures of MoS_2 and WS_2 [8]. This is explained by the fact that for all known transition metal dichalcogenides, methods for the synthesis of nanotubes with high yields and high crystallinity of the products, which exist for MoS_2 and WS_2 [8, 9], have not yet been developed. At the same time, it is known that tungsten diselenide has some advantages over disulfide. Diselenide is more stable and resistant to oxidation [10], and WSe_2 nanotube (NT) field-effect transistors are more productive and efficient [8, 11].

Several works are devoted to the experimental study of multi-walled nanotubes based on tungsten diselenide. One of the first methods to obtain stable WSe_2 NTs is considered in [12]. The starting material was commercial tungsten diselenide powder irradiated with electrons in an accelerator. The article [13] presents a high-resolution transmission electron microscopy (HRTEM) image of a four-walled nanotube. The authors of [14] synthesized WSe_2 nanotubes with diameters in the range of 300–1800 Å, with the maximum number of samples having a diameter of 900 Å.

The authors of [8] proposed a method for the synthesis of multi-walled WSe_2 NTs with significantly smaller diameters. The NTs obtained in [8] had diameters in the range of 100–400 Å, with an average value of 194 ± 54 Å. The authors report that the number of walls in the synthesized NTs varies from 4 to 20, with an average value of 9 ± 3. A HRTEM image of a five-walled nanotube has been published. The authors provide a graph of the relationship between the diameters of the observed NTs and the number of walls in them. It is reported that for the synthesized NTs, the graph shows a strong correlation between the NT diameter and the number of walls in them. The graph reveals that the outer diameter of the four-walled NTs is 100 Å, while the diameter of the five-walled NTs can vary in the range of 130–170 Å.

The authors of [15] report that the method developed by them for the synthesis of multi-walled WSe_2 NTs enables them to obtain a large yield of multi-walled NTs with the chirality angle equal for all nanotube walls. Such nanotubes among those synthesized

in [15] are the vast majority (75%). Among the NTs with the same chirality angle of the walls, achiral NTs are the most numerous: zigzag-type nanotubes (chirality angle 0°) account for 31%, and armchair-type nanotubes (chirality angle 30°) account for 26%. Chiral multi-walled NTs with the identical chiral wall angles of 17° ± 0.5° (8%) and 18° ± 0.5° (6%) are also distinguished.

Inorganic nanotubes are typically multi-walled [14], although single-walled NTs have been synthesized specifically for WS_2 by treating multi-walled NTs with high-energy plasma radiation in the radio range [16]. Due to computational limitations, ab initio quantum-chemical methods cannot be applied to tubes with more than 3 walls [15]. However, the structure, stability, thermodynamic and mechanical properties of multi-walled nanotubes at experimentally observed diameters can be modeled using force fields.

In this paper, we continue the investigation of the structure and energy properties of multi-walled NTs based on transition metal dichalcogenides, which was started in [17, 18]. Our study is based on molecular-mechanical modeling of multi-walled NTs using force fields. In this work, the force field describing the interactions between atoms in periodic WSe_2 nanosystems was developed using a genetic optimization algorithm [17].

One of the important features of the proposed force fields is the ability to account for interactions in layered systems. At least one other force field [19], capable of describing the interaction between layers and including a Kolmogorov-Crespi stacking-dependent term, has been presented in the literature. However, this field is intended to study relaxation effects, atomic reconstruction and corrugation in moiré-structured systems of transition metal dichalcogenide layers [19] and, to our knowledge, has never been used to model multi-walled NTs. At the same time, the parameterization of the force fields proposed in [17, 20] is based on databases containing the properties of single-walled NTs. This circumstance and the special techniques used in the development of the force field make it possible to increase its performance in the case of modeling multi-walled NTs.

The "Computational Details" section presents methods of quantum-chemical and molecular-mechanical calculations, the force field and the method of its calibration. This section also describes the main methods of creating NT models and calculating their energy characteristics.

The "Results and Discussion" section describes the process of testing the force field on single-walled (SWNT) and double-walled (DWNT) nanotubes by comparing the results of molecular-mechanical (MM) simulation with the results of quantum-chemical (QC) calculations. This section also discusses the results of using the obtained force field to simulate WSe_2 NTs with the number of walls from 1 to 6 and the outer diameter from 10 to 220 Å.

COMPUTATIONAL DETAILS

Quantum-chemical Calculations

In the present work, the quantum chemical calculations were performed for two purposes: first, to determine the physical properties of the test objects (see next section), for which there are currently no reliable experimental data, but which are necessary to calibrate the force field; second, the density functional theory (DFT) method was applied to selected single-walled and double-walled nanotubes to compare the ab initio calculated properties with those obtained by the force field method.

Quantum-chemical calculations were performed in the framework of density functional theory in accordance with the methodology adopted in our previous works [21–23]. The computer program CRYSTAL17 [24, 25], designed for modeling periodic systems, was used for the calculations. The basis of Bloch functions was constructed from Gaussian atomic orbitals. Relativistic CRENBL pseudopotentials [26, 27] were used to take into account the interaction between the Se core shells and valence electrons, as well as the interaction of the W core shells with valence and subvalence electrons.

The hybrid exchange-correlation functional HSE06 [28] was chosen to perform the calculations. Brillouin zone (BZ) summation was performed using Monkhorst-Pack grids [29] consisting of 18 × 18 × 10, 18 × 18, and 18 **k**-points for bulk WSe_2 crystals, nanolayers, and nanotubes, respectively. The one-electron equations were solved by the self-consistent field method with an energy accuracy of ~10^{-9} eV. To reproduce van der Waals interactions between monolayers in bulk crystals and multilayers, as well as between walls in multi-walled nanotubes (MWNTs), a dispersion correction in the DFT-D2 approximation was included in the calculations [30].

The presented technique has been successfully used previously to calculate the structural, electronic, and thermodynamic properties of SWNTs based on transition metal dichalcogenides [21–23]. It provides a reasonable compromise between accuracy and computational cost for systems containing hundreds of atoms per translation unit. A more detailed discussion of the technique employed can be found in the aforementioned articles [21–23].

Molecular-mechanical Calculations

In our previous works [17, 18], a new formulation of the SWMBL-C force field was proposed for the modeling of nanosystems based on transition metal disulfides. This potential model is basically identical to the one published in our earlier work [20] on the study of MoS_2 nanotubes. It includes five contributions: 1) the Coulomb potential, expressed in terms of the effective charges on the atoms; 2) the two-particle Morse potential, associated with the short-range W–

Se and W–W interactions; 3) the Buckingham potential, which conveys the pairwise interactions between the sulfur atoms; 4) the three-particle Stillinger-Weber potential, which specifies the contribution of the interactions associated with the WSeW valence angles; 5) an additional three-particle potential, which provides the energy difference between the trigonal prismatic and octahedral coordination of sulfur around the metal atom. The complete set of analytical expressions for these potentials is given in Table S1 in the Supplementary Information.

In the present work, the considered force field model is parameterized for nanosystems based on tungsten diselenide. As in [17, 18], the genetic algorithm with nondominated sorting (NSGA-III) [31] was used to parameterize the force field. It is a third generation genetic algorithm capable of solving multi-objective optimization problems with a large number of objectives. It utilizes a selection mechanism based on uniform distribution of solutions along the Pareto front [31] to maintain diversity and convergence of solutions. NSGA-III has several advantages over other multi-objective algorithms, such as scalability, reliability, and efficiency [32–34]. The parameter selection process is described in detail in our previous works [17, 18]. Based on the obtained data, a set of points is generated and used as an initial approximation for field fitting by the gradient descent algorithm implemented in the GULP program [35]. This program was also used for all molecular mechanics calculations.

The parameters of the force field were selected to reproduce the physical properties determined experimentally or calculated quantum-chemically for a limited number of calibration (training) systems. These systems included: 1) the most stable modification (2*H*) of the bulk crystal WSe_2; 2) a hypothetical unstable phase of the bulk crystal 1*T* with octahedral coordination of the W atoms; 3) a three-plane WSe_2 monolayer cut from a crystal with trigonal-pyramidal coordination of the W atoms; 4) five different bilayer polytypes formed by two parallel monolayers with different relative displacements and orientations; 5) two thin WSe_2 nanotubes with armchair (6, 6) and zigzag (12, 0) chirality.

The reference values of physical quantities comprised atomic coordinates, lattice parameters of 3D, 2D, and 1D periodic systems, sets of vibrational frequencies at the Γ, M, and K points of the BZ of the bulk crystal and the Γ point for the monolayer, elastic constants and moduli of the bulk phase, W–Se bond lengths, valence angles of WSeW and SeWSe, and relative energies of all systems included in the calibration set. It should also be noted that the values of the relative energies were determined as a result of quantum-chemical calculations. High accuracy of reproduction of these values is necessary to ensure the reliability of the results of modeling the stability of multi-walled nanotubes considered in the present work.

The charges on the W and Se atoms, which are the force field parameters, were calculated quantum-chemically by the method of Bader [36] as a result of the integration of the electron density of the bulk 2*H* WSe_2 crystal.

Nanotube Modeling

The initial structure of a single-walled nanotube was obtained from a WSe_2 (001) monolayer using the so-called folding procedure described in detail in the literature for carbon and other nanotubes with hexagonal morphology, starting from [37, 38]. A generalization to the case of nanolayers with arbitrary symmetry is given in [39] in the framework of the theory of line (helical) symmetry groups. A brief review of the terminology and the most important relations is given below.

The initial structure of a single-walled nanotube with a given precursor nanolayer composition can be uniquely defined by a pair of integer chirality indices n_1 and n_2 (it is assumed that $n_1 \geq n_2$). These two numbers define the chiral vector $\mathbf{R} = n_1\mathbf{a}_1 + n_2\mathbf{a}_2$ in the two-periodic lattice of the nanolayer with the principal translation vectors $\mathbf{a}_1$ and $\mathbf{a}_2$, which becomes the circumference of the cylindrical surface, in our case passing through the centers of the W atoms. If n is the greatest common divisor (GCD) for n_1 and n_2, then the chirality indices can be written as $n_1 = n\tilde{n}_1$; $n_2 = n\tilde{n}_2$. A set of nanotubes with the same reduced chirality $(\tilde{n}_1, \tilde{n}_2)$ have collinear chiral vectors $R = n\tilde{R}$ directed along a ray $\tilde{R} = \tilde{n}_1\mathbf{a}_1 + \tilde{n}_2\mathbf{a}_2$ in the Bravais lattice of the monolayer. In the case of a hexagonal two-periodic lattice with an angle between the principal vectors of 60° (which will be assumed everywhere in the following), the magnitude of the reduced chiral vector $\tilde{R}$ can be found from the relation:

$$\tilde{R} = a\sqrt{\tilde{n}_1^2 + \tilde{n}_1\tilde{n}_2 + \tilde{n}_2^2}, \quad (1)$$

where a is the parameter of the 2D hexagonal lattice. Consequently, the initial NT diameter (before optimization) can be expressed by the ratio:

$$D_{\mathrm{NT}} = n\tilde{R}/\pi. \quad (2)$$

Using the orthogonality relation [37–39] between the reduced chirality vector and the nanotube translation vector $\mathbf{T}$ $\left(\tilde{R}\cdot T = 0\right)$, we can determine the magnitude of the initial period of the nanotube T_{NT}:

$$T_{\mathrm{NT}} = |\mathbf{T}| = \frac{\sqrt{3}}{\tau}\tilde{R}, \quad (3)$$

where

$$\tau = \begin{cases} 1(\tilde{n}_1 - \tilde{n}_2) \bmod 3 \neq 0 \\ 3(\tilde{n}_1 - \tilde{n}_2) \bmod 3 = 0. \end{cases} \quad (4)$$

Nanotubes with the same chirality indices have the same chiral angle θ, which is defined as the angle between the vectors $\tilde{\mathbf{R}}$ and $\mathbf{a}_1$. This angle is completely determined by the ratio $\rho = \tilde{n}_2/\tilde{n}_1$:

$$\theta = \arctan\frac{\sqrt{3}\rho}{2+\rho}. \quad (5)$$

The specified set of nanotubes is called SCANT (single chirality angle nanotubes) [15]. The limits of chiral angle variation are determined by its value for achiral nanotubes. These values are 0° for (n, 0) zigzag type NTs and 30° for (n, n) armchair type NTs. The intermediate values of θ correspond to chiral nanotubes (Fig. S1).

In the present work, the initial geometry of multi-walled nanotubes was obtained by coaxial superposition of single-walled SCANT components of different diameters. All components of the SWNTs were folded from a single monolayer and combined without twisting and shifting, resulting in a 3R packing of single-walled components [2, 18]. In selecting a set of single-walled components for a given MWNT, three requirements were met: the first is the SCANT condition, which automatically ensures a common translational period for all walls; the second concerns the initial interwall distances (i.e. the distances between adjacent cylindrical surfaces of W atoms), which were chosen in the range of 6.0 to 7.0 Å, approximately corresponding to the interlayer distance in a bulk WSe_2 crystal. This was achieved by selecting an appropriate chirality index difference (Δn_{NT}) between the adjacent single-walled components. Finally, the third requirement was that the GCD of the chirality indices should be as large as possible to maximize the axial symmetry of the MWNTs. The last condition has been used mainly in quantum-chemical calculations of double- and triple-walled nanotubes, but not in force field modeling.

Two energy criteria have been used to analyze the stability of multi-walled nanotubes. The first is the binding energy (E_{bind}), which reflects the energy gain when several SWNTs are combined into a single MWNT. For an N-walled nanotube, it is determined by the relation:

$$E_{bind} = \left(E_{MWNT} - \sum_{i=1}^{N} E_{SWNT_i}\right) \Big/ N_{MWNT}, \quad (6)$$

where E_{MWNT} and E_{SWNT_i} are the total energies per primitive cell of the MWNT and the i-th single-walled component, respectively, and N_{MWNT} is the number of WSe_2 formula units in the MWNT primitive cell. The second property (E_{str}) is the energy of formation of a nanotube with n_w walls from a WSe_2 nanolayer that contains n_w monolayers [40]:

$$E_{str} = E_{MWNT}/N_{MWNT} - E_{n_w-layer}/N_{n_w-layer}, \quad (7)$$

where $E_{n_w-layer}$ and $N_{n_w-layer}$ are the total energy and the number of formula units in a primitive 2D cell of the nanolayer consisting of n_w monolayers. The nanolayers used were cut from the stable 3R polytype of the bulk WSe_2 crystal. The E_{str}, calculated by formula (7), characterizes the energy effect for the hypothetical folding of nanolayers into multi-walled nanotubes and is analogous to the strain energy for single-walled nanotubes, which coincides with it at $n_{wr} = 1$.

RESULTS AND DISCUSSION

Testing the Proposed Force Field

Strain energies are traditionally used to evaluate the stability of single-walled nanotubes. Figure 1 shows the folding energies obtained both non-empirically (using the DFT method) and using the proposed force field. To illustrate the differences between tungsten disulfide and tungsten diselenide, Fig. 1a compares the non-empirical data for WS_2 obtained in [17] and the present results for WSe_2. As can be seen from the figure, E_{str} for WSe_2 nanotubes is slightly higher (by ~20%) than for WS_2 nanotubes, indicating that the stability of the former NTs is lower than that of the latter. Molecular mechanics calculations of the strain energy of single-walled achiral WSe_2 nanotubes showed good agreement with the results of the DFT method (Fig. 1b). Only a small (~2%) overestimation of the force field results is observed. At the same time, both approaches show that the stability of SWNTs is mainly determined by the nanotube diameter and weakly dependent on the chirality angle.

In this work, non-empirical modeling of a number of achiral double-walled nanotubes has been performed. Figure 2 shows a cross section of two nanotubes with close diameters but different chirality as an example of optimized structures. A comparison between the results obtained by the force field method and the quantum chemical data for the selected nine double-walled NTs is presented in Table 1. This table summarizes the binding energies E_{bind}, strain energies E_{str}, periods T_{NT}, diameters D_{NT} and interwall distances ΔR_{NT} for the nine achiral double-walled tubes (cross sections of two tubes of different chirality are shown in Fig. S2). The data in Table 1 indicate a good quality of the force field. The deviations of periods, average diameters and interwall distances in the nanotubes from non-empirical values do not exceed 0.5 Å in most cases. The error of the binding energies is <1 kJ/mol.

Figure 3 shows the dependence of the binding energies on the interwall distance. The presence of minima on the plotted curves suggests that, at least for double-walled nanotubes, there is an optimal wall distance. From the data obtained, this distance is close to 6.5 Å for both types of chirality, which roughly corresponds to a difference in chirality indices Δn_{NT} of 7 and 13 for armchair and zigzag nanotubes, respec-

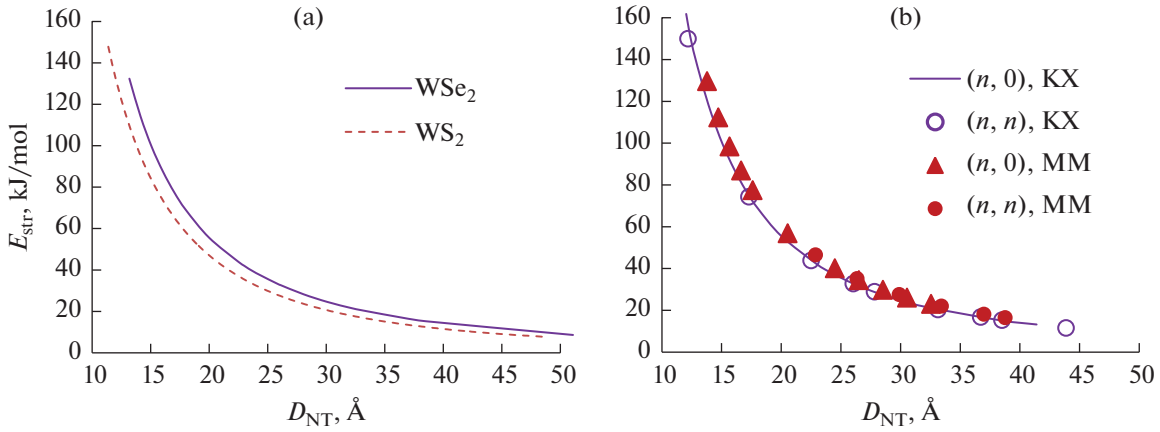

Fig. 1. Dependence of the calculated strain energies of single-walled achiral nanotubes on their diameter: (a)—comparison of the results of quantum-chemical calculations for WSe_2 and WS_2 nanotubes (common curves for two chiralities); (b)—comparison of the results of quantum-chemical and molecular-mechanical calculations for WSe_2. Designations: MM—results of force field calculations; QC—results of quantum-chemical calculations.

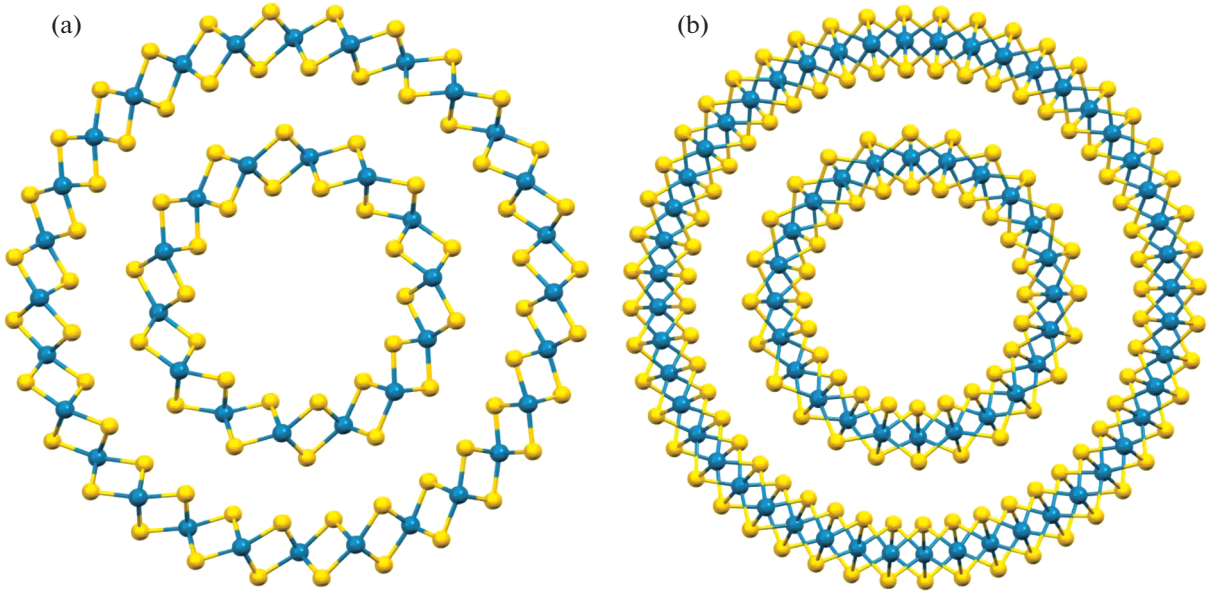

Fig. 2. Cross section of double-walled WSe_2 nanotubes: (a) – armchair tube (7, 7)@(14, 14); (b) – zigzag tube (12, 0)@(24, 0). Results of quantum-chemical calculations. Light spheres are Se atoms, dark spheres are W atoms.

tively. Similar values were obtained for tungsten disulfide based nanotubes in [17, 18]. Nevertheless, the average interwall distance in WSe_2 nanotubes is ~0.3 Å larger than that in WS_2 nanotubes and practically coincides with the value of the interlayer distance in the bulk 2*H* phase WSe_2 (6.49 Å) [41].

Calculations of Multi-walled Nanotubes

The choice of MWNTs for molecular-mechanical modeling in the present work is mainly dictated by the fact that one of its goals is to compare the properties of WSe_2 and WS_2 MWNTs. Therefore, the same key objects that were previously studied in the case of tungsten disulfide [17, 18] were chosen for the modeling of tungsten diselenide MWNTs. A sequence of six nanotubes from single-walled (142, 0) to six-walled (142, 0)@(154, 0)@(142, 0)@(154, 0)@(142, 0)@(154, 0)@(166, 0)@(178, 0) with a constant difference in chirality indices of neighboring walls $\Delta n_{NT} = 12$ was considered for zigzag chirality. A sequence of six tubes from single-walled (84, 84) to six-walled (84,

Table 1. Computational results of the properties of double-walled WSe_2 nanotubes. QC – DFT results, MM – force field results. See text for definition of included quantities

Chirality	Δn_{NT}	E_{bind}, kJ/mol		E_{str}[a], kJ/mol		Nanotube period, T_{NT}, Å		Average diameter, D_{NT}[b], Å		Interwall distance, ΔR_{NT}[c], Å	
(n, n)	–	QC	MM	QC	MM	QC	MM	QC	MM	QC	MM
(12, 12)@(18, 18)	6	−5.1	−5.8	38.2	40.0	3.30	3.30	28.2	28.5	6.3	6.3
(14, 14)@(21, 21)	7	−10.9	−11.9	24.9	26.0	3.29	3.30	32.4	32.6	6.5	6.5
(12, 12)@(20, 20)	8	−10.9	−11.2	29.6	31.4	3.29	3.30	29.5	29.8	6.8	6.7
(12, 12)@(21, 21)	9	−6.3	−6.7	32.9	34.6	3.29	3.31	30.3	30.6	7.2	7.3
$(n, 0)$	–	KX	MM	KX	MM	KX	MM	KX	MM	KX	MM
(11, 0)@(22, 0)	11	−5.9	−6.0	77.5	77.8	5.61	5.55	18.9	19.4	6.0	6.0
(12, 0)@(24, 0)	12	−10.7	−11.1	62.8	63.1	5.63	5.58	20.2	20.7	6.2	6.2
(13, 0)@(26, 0)	13	−11.8	−12.1	53.8	54.5	5.64	5.60	21.5	22.1	6.5	6.4
(14, 0)@(28, 0)	14	−10.2	−10.4	49.0	49.9	5.64	5.61	22.9	23.5	6.8	6.7
(15, 0)@(30, 0)	15	−7.5	−7.5	46.3	47.6	5.65	5.62	24.4	24.9	7.1	7.1

[a] Energy of formation with respect to the bilayers.
[b] Sum of the average radial distances to W atoms in the inner and outer walls.
[c] Difference of average radial distances to atoms W in outer and inner walls.

84)@(91, 91)@(98, 98)@(105, 105)@(112, 112)@(119, 119) with chirality step $\Delta n_{NT} = 7$ is also considered for armchair chirality.

A sequence of five chiral nanotubes with $\rho = 1/2$ and chiral angle $\theta = 19.11°$ (80, 40), ... (80, 40)@(88, 44)@(98, 49)@(106, 53)@(116, 58) is characterized by variable values of the difference of the first chirality indices of the adjacent walls 8 and 10, which is related to the difficulty to provide the initial interwall distance in chiral nanotubes that is close to the interlayer gap in the bulk crystal. As the wall number i increase, the values of $(n_{i+1} - n_i)$ alternate: 8, 10, 8, 10, etc. MWNTs with this structure have slightly different properties than MWNTs generated with a constant value of Δn_{NT}, but such a non-constant chirality step after geometry optimization leads to tubes with a uniform interwall gap.

The interwall distance ΔR_{NT} is an important structural parameter of multi-walled nanotubes. This parameter has been measured in nanotubes of WSe_2 composition in at least four works. The earliest study [12] found the value of $\Delta R_{NT} = 6.588$ Å, papers [13, 42] presented the values of $\Delta R_{NT} = 6.5$ and 6.569 Å, respectively, and a relatively recent study [14] obtained the value of $\Delta R_{NT} = 6.7$ Å. Our molecular-mechanical modeling predicts that among all the MWNTs studied

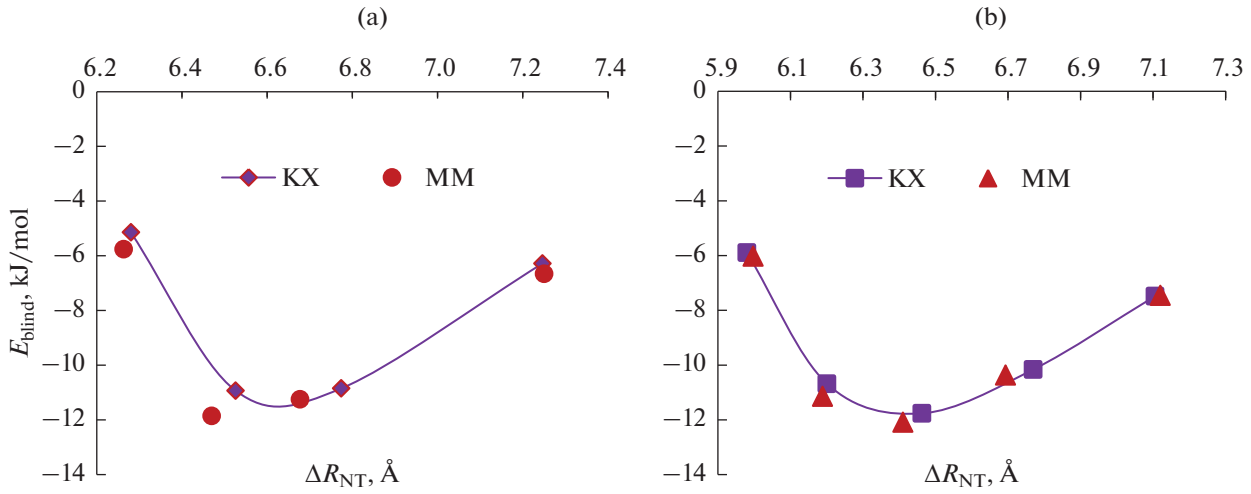

Fig. 3. Dependence of the binding energy of double-walled achiral nanotubes on the value of the interwall distance: (a)—armchair tubes; (b)—zigzag tubes. Designations: MM—results of force field calculations; QC—results of quantum-chemical calculations. The points marked on the plots correspond to the chiralities given in the first column of Table 1.

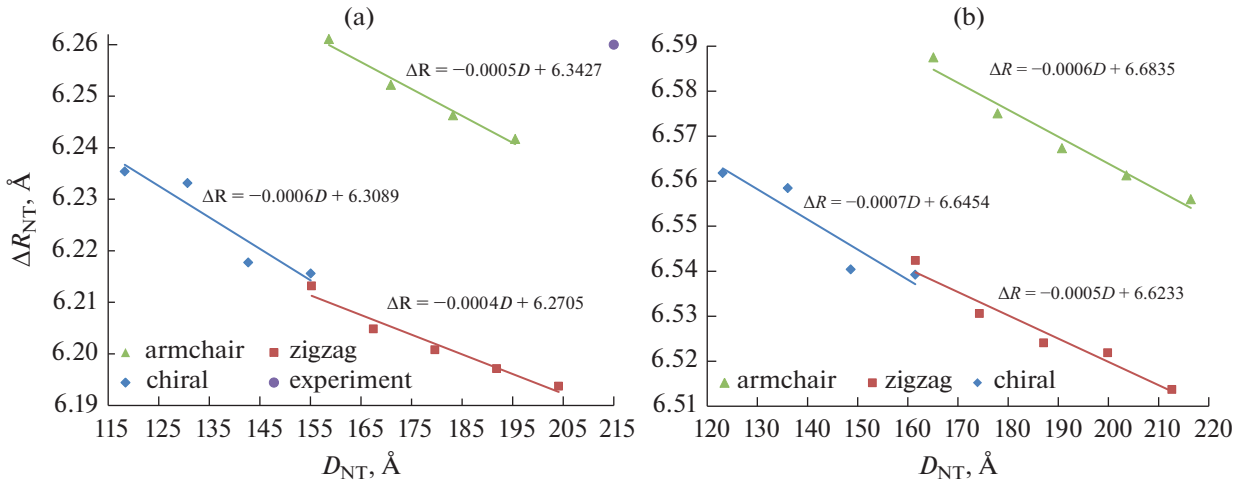

Fig. 4. Dependence of the average interwall distance on the outer diameter for MWNTs: (a)—WS_2 (experimental value for an armchair nanotube from [8]); (b)—WSe_2. Straight lines correspond to linear approximations $\Delta R_{NT}(D_{NT}) = a + bD_{NT}$, whose coefficients are also shown in the figures.

in the present work, the smallest value of $\Delta R_{NT} = 6.505$ Å can occur in a six-walled WSe_2 NT of zigzag type between the third and fourth walls, and the largest value of $\Delta R_{NT} = 6.562$ Å is possible in a double-walled chiral ($\theta = 19.11°$) WSe_2 NT. Thus, the largest value of the interwall distance predicted by the model is very close to the smallest measured value of this parameter. The value of the interwall distance in WS_2 MWNTs is smaller than that in WSe_2 nanotubes. In the case of WS_2 multi-walled nanotubes, the measurements lead to interwall distance values in the range of 6.214–6.250 Å [6, 7] and 5.950–6.420 Å [8].

Our simulation results show that the MWNTs of WSe_2 and WS_2 with the same chirality have larger diameters in WSe_2 nanotubes. The calculated outer diameters of six-walled NTs of armchair chirality are $D_{NT} = 204$ Å for WS_2 and 216 Å for WSe_2. For zigzag chirality, $D_{NT} = 204$ Å for WS_2 and 213 Å for WSe_2. The outer diameters of the five-walled chiral NTs with $\theta = 19.11°$ are $D_{NT} = 155$ Å for WS_2 and 162 Å for WSe_2.

In the experimental work [8], the dependence of the interwall distance on the outer diameter of multi-walled WS_2 nanotubes was obtained. Our data are in qualitative agreement with the results reported in [8]. In the present work, we compare the intensity of the decrease of the average interwall distance with increasing outer diameter for WSe_2 MWNTs with the same value for WS_2. In Fig. 4, we present the $\Delta R_{NT}(D_{NT})$ dependencies for nanotubes of three chiralities. Each $\Delta R_{NT}(D_{NT})$ dependence is approximated by a linear regression $\Delta R_{NT} = a_i + b_i \cdot D_{NT}$, where i denotes the chirality type. The regression coefficients b_i correspond to the derivatives $\partial \Delta R_{NT}/\partial D_{NT}$ and their values are given in the same figure. It can be seen that the indicated parameters are very close for WSe_2 and WS_2 NTs, but the absolute value of b_i for WSe_2 NTs is slightly higher than b_i for WS_2 NTs. The experimental data [8] are plotted with a single point in Fig. 4, since the other values in [8] are obtained for much larger diameters of WS_2 MWNTs than those modeled in this work.

It is known from experimental observations [43] that the magnitude of the interwall distance depends on the location of the walls inside the nanotube. The initial MWNT model, let us call it precursor, consists of unoptimized single-walled nanotubes nested inside each other. In the armchair MWNT precursors, a constant chirality index difference $\Delta n_{NT} = 7$ corresponds to a constant initial interwall distance $\Delta R^0_{NT} = 6.34$ Å, while for the zigzag chirality MWNT precursors a constant $\Delta n_{NT} = 12$ corresponds to $\Delta R^0_{NT} = 6.27$ Å. These interwall distances are smaller than the interwall distance in the bulk $2H$ phase of WSe_2 (6.49 Å) [41]. With this choice of precursors, the results of our MWNT simulation show that the value of ΔR_{NT} is maximal for the innermost walls. As we approach the MWNT surface, the value of ΔR_{NT} decreases, reaches a minimum, and starts to increase, but does not reach the maximum value observed for the innermost walls. This behavior of ΔR_{NT} is characteristic of both WS_2 MWNTs [18] and WSe_2 MWNTs. However, the ΔR_{NT} values themselves and their variations are larger for WSe_2 MWNTs. In the six-walled WSe_2 MWNT of zigzag type, the maximum value of interwall distance $\Delta R_{NT} = 6.531$ Å is observed between the innermost and second wall, while the minimum value $\Delta R_{NT} = 6.505$ Å is observed between the 4th and 5th wall. In the six-walled WS_2 zigzag MWNT, the maximum value of $\Delta R_{NT} = 6.207$ Å is observed between the innermost and

second wall, while the minimum value of ΔR_{NT} = 6.187 Å is observed between the 4th and 5th wall.

The chiral MWNT precursors utilize a structure of interleaved Δn_{NT} values, which naturally leads to two alternating initial values of the interwall distances. For WSe_2 nanotube precursors with chiral angle θ = 19.11°, the chirality index difference Δn_{NT} = 8 corresponds to ΔR^0_{NT} = 5.53 Å, while Δn_{NT} = 10 corresponds to ΔR^0_{NT} = 6.91 Å.

Optimization of the precursor structure using the developed force field leads to the following result. In a five-walled WSe_2 NT with θ = 19.11°, ΔR_{NT} = 6.547 Å for the innermost walls. As one moves towards the MWNT surface, the value of ΔR_{NT} decreases to a minimum (6.513 Å). For the 4th and 5th walls, ΔR_{NT} increases sharply to a maximum value (6.553 Å). In the five-walled WS_2 NT, there is a similar distribution of interwall distances along the thickness of the NT. The innermost and outermost walls have the largest interwall distances: between the 1st and 2nd walls is 6.224 Å, between the 4th and 5th walls is 6.223 Å, and the minimum is 6.194 Å.

Another important aspect of multi-walled nanotube structure is the shape of single-walled MWNT components. In several previous works [44, 20], we found a deviation of the shape of the outer walls of MWNTs from perfectly cylindrical to partially faceted. In one of our earlier works [45], we proposed a simple function η(φ) that reflects the deviation of atomic positions from their location on a perfectly cylindrical surface:

$$\eta(\varphi) = \frac{R_A(\varphi)}{\langle R_A \rangle} - 1, \quad (8)$$

where $R_A(\varphi)$ is the radial distance from the tube axis to the center of atom A, φ is the azimuthal angle in the cylindrical coordinate system, and $\langle R_A \rangle$ is the average value of $R_A(\varphi)$ over all atom positions in a given shell (wall).

The analysis based on the calculation of the above function showed that, regardless of the composition, the faceting effect is most pronounced for armchair nanotubes and has at least an order of magnitude smaller amplitude for zigzag MWNTs. Chiral tubes may occupy an intermediate position. The degree of faceting increases with increasing diameter and grows from the inner walls to the outer walls.

Figure 5 provides a comparison of the cylindricity deviation function η(φ) for the outer walls of five-walled armchair (84, 84)@(91, 91)@(98, 98)@(105, 105)@(112, 112) and chiral (80, 40)@(88, 44)@(98, 49)@(106, 53)@(116, 58) NTs calculated by the force field method for WS_2 and WSe_2. The cross sections of the above tubes are presented in Figs. S2a, S2c, S3a, S3c. Figure 5a clearly shows that for the armchair tube, the results for tungsten disulfide and tungsten diselenide are almost the same. The functions obtained have a characteristic period equal to $2\pi/\Delta n_{NT}$ (~51.4° при Δn_{NT} = 7), indicating a potentially heptagonal structure. The faceted nature of MWNTs has been substantiated in [46] by analyzing the interlayer packing patterns in carbon and boron nitride multi-walled nanotubes. The authors of [46] found that above a certain critical diameter, achiral MWNTs exhibit evenly spaced axial faces, the number of which is actually equal to the difference in the chirality indices of the adjacent walls. This conclusion is in good agreement with our results.

The chiral nanotube (Figs. S2c, S3c) exhibits approximately the same degree of deviation from cylindricity as the armchair nanotube, but the function η(φ) has no pronounced periodicity. This indicates that its shape does not correspond to a regular polyhedron, possibly due to the method of precursor construction for this tube discussed above, which uses interleaved values of Δn_{NT}.

The outer walls of the WS_2 and WSe_2 zigzag tubes of chirality (142, 0)@(154, 0)@(142, 0)@(154, 0)@(154, 0)@(166, 0) have deviations from periodicity that are an order of magnitude smaller than for the two tubes considered above. Therefore, we have not included the dependence η(φ) for them in Fig. 5, but their cross section is shown in Figs. S2b, S3b.

Figures 6, 7 show the dependence of the binding energy E_{bind} (formula (6)) and the strain energy E_{str} (formula (7)) on the number of walls in multi-walled WS_2 and WSe_2 nanotubes. These two quantities correspond to two different effects: 1) nanotube stabilization due to interwall interactions, and 2) destabilization due to deformation of the nanolayers during folding.

As can be seen from Fig. 6, the $E_{bind}(n_w)$ curves for WSe_2 nanotubes are ~4 kJ/mol lower than those for WS_2 nanotubes in the large diameter region. Thus, the stabilizing interaction between the walls is stronger in WSe_2 MWNTs than in WS_2 MWNTs, probably due to the greater intensity of van der Waals forces between bulkier Se atoms. For the considered models of WSe_2 and WS_2 MWNTs, the $E_{bind}(n_w)$ curves for the zigzag chirality are slightly below the curves for the other types of chirality for the same composition; this correlates with the fact that the interwall distances in zigzag MWNTs are the smallest (Fig. 4).

As indicated in Fig. 7, the energy of MWNT formation from multilayers for chiral MWNTs of WS_2 and WSe_2 does not differ much (in tenths of kJ/mol), while it is almost the same for achiral MWNTs. This is mainly due to the fact that in the diameter range of 100–200 Å the strain energy of single-walled nanotubes is small, being of the order of 1–2 kJ/mol for nanotubes of both compositions. As the number of walls increases, the $E_{str}(n_w)$ curves reach a plateau in

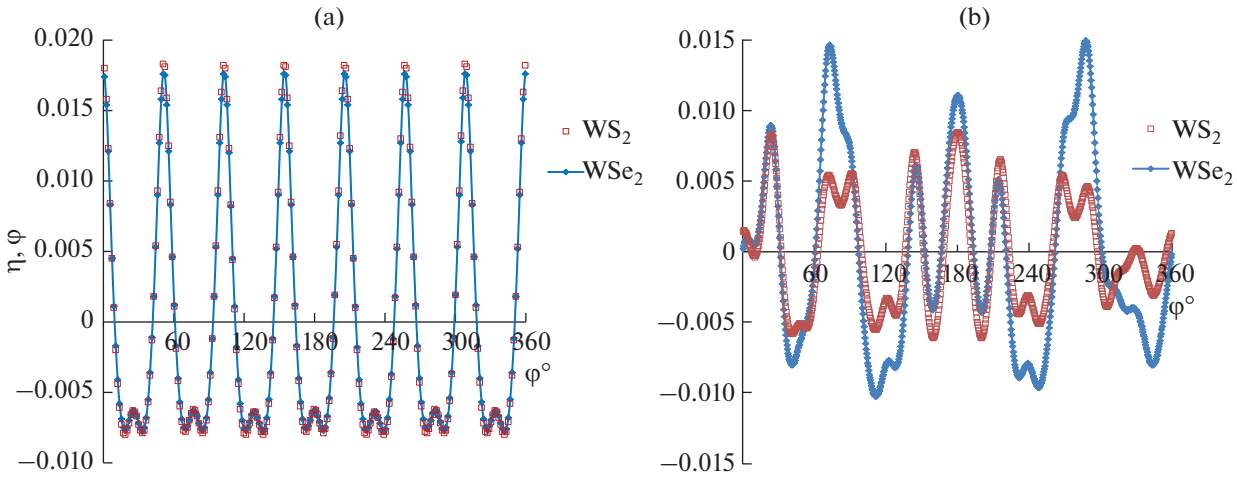

Fig. 5. Cylindricity deviation function η(φ) for the outer walls of five-walled WS_2 and WSe_2 nanotubes: (a)—η function for armchair NT (84, 84)@(91, 91)@(98, 98)@(105, 105)@(112, 112); (b)—η function for chiral NT (80, 40)@(88, 44)@(98, 49)@(106, 53)@(116, 58).

the range of n_w from 3 to 6. However, the energies of MWNT formation from nanolayers differ noticeably for different types of chirality. They decrease in the order chiral > armchair > zigzag for both WSe_2 and WS_2.The larger E_{str} values for chiral tubes are most likely due to the smaller values of the diameters of the considered MWNTs compared to the diameters of achiral tubes (Fig. 4). The differences between armchair and zigzag MWNTs seem to be due to their different geometric structure. Due to the distortion of the wall shape towards facetedness, the armchair tubes have a more lax structure, which, as can be clearly seen in Fig. 4, is expressed in large average interwall distances.

CONCLUSIONS

A force field for modeling nanotubes based on layered modifications of tungsten diselenide has been proposed. The parameters of the force field were adjusted on layered polytypes of bulk crystals, monolayers, bilayers, and small-diameter nanotubes. Comparison with the results of quantum-chemical calculations confirmed that the proposed field well reproduces the strain energies of single-walled nanotubes, as well as the binding and strain energies of double-walled nanotubes. In addition, the force field satisfactorily reproduces the periods, diameters, and interwall distances of double-walled nanotubes.

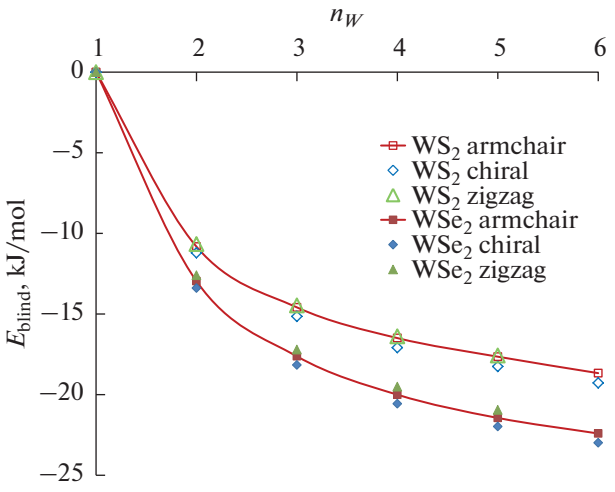

Fig. 6. Dependence of the binding energy (E_{bind}) on the number of walls in multi-walled WS_2 and WSe_2 nanotubes. Molecular-mechanics data for achiral (armchair and zigzag) and chiral nanotubes are presented.

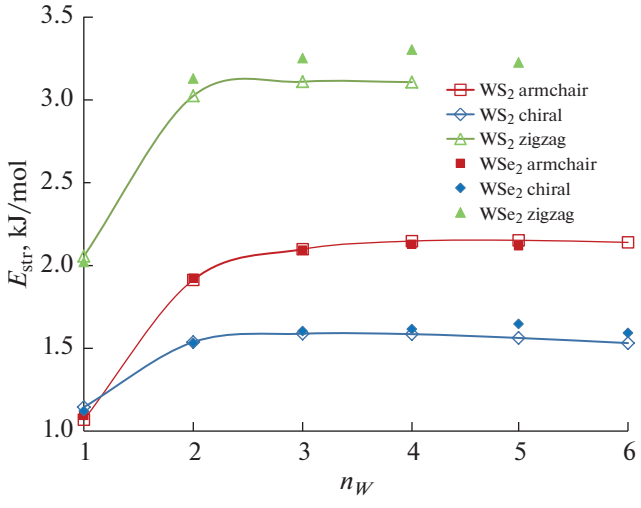

Fig. 7. Dependence of the energy of formation from multilayers (E_{str}) on the number of walls in multi-walled WS_2 and WSe_2 nanotubes. The data for achiral (armchair and zigzag) and chiral nanotubes obtained by molecular mechanics are presented.

The choice of specific multi-walled nanotubes for molecular-mechanical modeling in the present work was dictated by the fact that one of its goals was to compare the properties of WSe_2 and WS_2 MWNTs. Therefore, the same key objects that were previously studied in the case of tungsten disulfide were chosen for the modeling of tungsten diselenide MWNTs.

The analysis of the deviations of the shape of the walls of the considered nanotubes from the cylindrical surface shows that, for both compositions, the largest deviation towards facetedness is observed for the armchair nanotubes and the considered chiral nanotubes. The observed distortions are one order of magnitude smaller for the zigzag nanotubes.

Calculations have shown that among the considered multi-walled nanotubes of the same diameter, zigzag tubes are the most stable with respect to the corresponding WSe_2 and WS_2 nanolayers, while chiral tubes are less stable than achiral ones. The calculated interwall distances for the studied models are in good agreement with the available experimental data, being ~0.3 Å larger for WSe_2 nanotubes. Nevertheless, the stabilizing contribution of the interwall interaction is larger in WSe_2 MWNTs than in WS_2 MWNTs, probably due to the greater intensity of van der Waals forces between bulkier and more polarizable Se atoms.

SUPPLEMENTARY INFORMATION

The online version contains supplementary material available at https://doi.org/10.1134/S003602362460268X.

ACKNOWLEDGMENTS

The authors are grateful to the Resource Center "Computer Center of St. Petersburg State University" for the provision of computing facilities and assistance in the realization of high-producible calculations.

FUNDING

This work was financially supported by the Russian Science Foundation (RSF) under the research project No. 23-23-00040, https://rscf.ru/project/23-23-00040/.

CONFLICT OF INTEREST

The authors of this work declare that they have no conflicts of interest.

REFERENCES

1. J. L. Musfeldt, Y. Iwasa, and R. Tenne, Phys. Today **73**, 42 (2020). https://doi.org/10.1063/PT.3.4547
2. M. Bar-Saden and R. Tenne, Nat. Mater. **23**, 310 (2024). https://doi.org/10.1038/s41563-023-01609-x
3. A. Jorio, G. Dresselhaus, and M. S. Dresselhaus, *Carbon Nanotubes: Advanced Topics in the Synthesis, Structure, Properties and Applications* (Springer, Berlin, 2008).
4. J. R. Schaibley, H. Yu, G. Clark, et al., Nat. Rev. Mater. **1**, 16055 (2016). https://doi.org/10.1038/natrevmats.2016.55
5. Y. Yomogida, Y. Miyata, and K. Yanagi, Appl. Phys. Express **12**, 085001 (2019). https://doi.org/10.7567/1882-0786/ab2acb
6. X. Heming, C. Xinyu, L. Song, et al., Nano Lett. **21**, 4937 (2021). https://doi.org/10.1021/acs.nanolett.1c00497
7. Y. Sun, S. Xu, Z. Xu, et al., Nat. Commun. **13**, 5391 (2022). https://doi.org/10.1038/s41467-022-33118-x
8. Y. Yomogida, Y. Kainuma, T. Endo, et al., Appl. Phys. Lett. **116**, 203106 (2020). https://doi.org/10.1063/5.0005314
9. S. S. Sinha, L. Yadgarov, S. B. Aliev, et al., J. Phys. Chem. C **125**, 6324 (2021). https://doi.org/10.1021/acs.jpcc.0c10784
10. S. Kumar and U. Schwingenschlögl, Chem. Mater. **27**, 1278 (2015). https://doi.org/10.1021/cm504244b
11. H.-J. Chuang, X. Tan, N. J. Ghimire, et al., Nano Lett. **14**, 3594 (2014). https://doi.org/10.1021/nl501275p
12. D. H. Galván, R. Rangel, and E. Adem, Fullerene Sci. Technol. **9**, 15 (2000). https://doi.org/10.1080/10641220009351392
13. H. Kim, S. J. Yun, J. C. Park, et al., Small **11**, 2192 (2015). https://doi.org/10.1002/smll.201403279
14. M. B. Sreedhara, Y. Miroshnikov, K. Zheng, et al., J. Am. Chem. Soc. **144**, 10530 (2022). https://doi.org/10.1021/jacs.2c03187
15. Q. An, W. Xiong, F. Hu, et al., Nat. Mater. **23**, 347 (2024). https://doi.org/10.1038/s41563-023-01590-5
16. S. Ghosh, V. Brüser, I. Kaplan-Ashiri, et al., Appl. Phys. Rev. **7**, 041401 (2020). https://doi.org/10.1063/5.0019913
17. A. V. Bandura, S. I. Lukyanov, A. V. Domnin, et al., Russ. J. Inorg. Chem. **68**, 1582 (2023). https://doi.org/10.1134/S003602362360209X
18. A. V. Bandura, S. I. Lukyanov, A. V. Domnin, et al., Comput. Theor. Chem. **1229**, 114333 (2023). https://doi.org/10.1016/j.comptc.2023.114333
19. C. E. M. Nielsen, M. Cruz, A. Torche, et al., Phys. Rev. B **108**, 045402 (2023). https://doi.org/10.1103/PhysRevB.108.045402
20. A. V. Bandura, S. I. Lukyanov, D. D. Kuruch, et al., Physica E **124**, 114183 (2020). https://doi.org/10.1016/j.physe.2020.114183
21. R. A. Evarestov, A. V. Bandura, V. V. Porsev, et al., J. Comput. Chem. **38**, 2581 (2017). https://doi.org/10.1002/jcc.24916
22. R. A. Evarestov, A. V. Kovalenko, A. V. Bandura, et al., Mater. Res. Express **5**, 115028 (2018). https://doi.org/10.1088/2053-1591/aadf00

23. R. A. Evarestov, A. V. Kovalenko, A. V. Bandura, et al., Physica E **115**, 113681 (2020). https://doi.org/10.1016/j.physe.2019.113681
24. R. Dovesi, A. Erba, R. Orlando, et al., WIREs Comput. Mol. Sci. **8**, e1360 (2018). https://doi.org/10.1002/wcms.1360
25. R. Dovesi, V. R. Saunders, C. Roetti, et al., *CRYSTAL17 User's Manual* (University of Turin, Torino, 2018).
26. L. F. Pacios and P. A. Christiansen, J. Chem. Phys. **82**, 2664 (1985). https://doi.org/10.1063/1.448263
27. R. B. Ross, J. M. Powers, T. Atashroo, et al., J. Chem. Phys. **93**, 6654 (1990). https://doi.org/10.1063/1.458934
28. J. Heyd, G. E. Scuseria, and M. Ernzerhof, J. Chem. Phys. **118**, 8207 (2003). https://doi.org/10.1063/1.1564060
29. H. J. Monkhorst and J. D. Pack, Phys. Rev. B **13**, 5188 (1976). https://doi.org/10.1103/PhysRevB.13.5188
30. S. Grimme, J. Comput. Chem. **27**, 1787 (2006). https://doi.org/10.1002/jcc.20495
31. K. Deb and H. Jain, IEEE Trans. Evol. Comput. **18**, 577 (2014). https://doi.org/10.1109/TEVC.2013.2281535
32. R. H. Bhesdadiya, I. N. Trivedi, P. Jangir, et al., Cogent Eng. **3**, 1269383 (2016). https://doi.org/10.1080/23311916.2016.1269383
33. X. Xue, J. Lu, and J. Chen, CAAI Trans. Intelligence Technol. **4**, 135 (2019). https://doi.org/10.1049/trit.2019.0014
34. L. Chen, Q. Gu, R. Wang, et al., Sustainability **14**, 10766 (2022). https://doi.org/10.3390/su141710766
35. J. D. Gale and A. L. Rohl, Mol. Simul. **29**, 291 (2003). https://doi.org/10.1080/0892702031000104887
36. R. F. W. Bader, Acc. Chem. Res. **18**, 9 (1985). https://doi.org/10.1021/ar00109a003
37. R. A. Jishi, M. S. Dresselhaus, and G. Dresselhaus, Phys. Rev. B **47**, 16671 (1993). https://doi.org/10.1103/physrevb.47.16671
38. E. B. Barros, A. Jorio, G. G. Samsonidze, et al., Phys. Rep. **431**, 261 (2006). https://doi.org/10.1016/j.physrep.2006.05.007
39. M. Damnjanović, B. Nikolić, and I. Milošević, Phys. Rev. B **75**, 033403 (2007). https://doi.org/10.1103/PhysRevB.75.033403
40. N. L. Marana, Y. Noel, J. R. Sambrano, et al., J. Phys. Chem. A **125**, 4003 (2021). https://doi.org/10.1021/acs.jpca.1c01682
41. M. A. T. Nguyen, A. S. Gupta, J. Shevrin, et al., RSC Adv. **8**, 9871 (2018). https://doi.org/10.1039/c8ra01497c
42. K. Xu, F. Wang, Z. Wang, et al., ACS Nano **8**, 8468 (2014). https://doi.org/10.1021/nn503027k
43. M. Krause, A. Mücklich, A. Zak, et al., Phys. Status Solidi B **248**, 2716 (2011). https://doi.org/10.1002/pssb.201100076
44. A. V. Bandura and R. A. Evarestov, J. Comput. Chem. **35**, 395 (2014). https://doi.org/10.1002/jcc.23508
45. A. V. Bandura and R. A. Evarestov, Surf. Sci. **641**, 6 (2015). https://doi.org/10.1016/j.susc.2015.04.027
46. I. Leven, R. Guerra, A. Vanossi, et al., Nature Nanotech. **11**, 1082 (2016). https://doi.org/10.1038/nnano.2016.151

Publisher's Note. Pleiades Publishing remains neutral with regard to jurisdictional claims in published maps and institutional affiliations.
AI tools may have been used in the translation or editing of this article.

SPELL: OK